

# Modelling of CSTR Flow Field for Agaricus bisporus Residue Fermentation Based on CFD Numerical Simulation

Jiayu Li (✉ [gayu1020@163.com](mailto:gayu1020@163.com))

Fujian Agriculture and Forestry University

Xuan Wei

Fujian Agriculture and Forestry University <https://orcid.org/0000-0002-8522-1886>

Jinping Zou

Fujian Agriculture and Forestry University

---

## Research Article

**Keywords:** Biogas, Computational fluid dynamics (CFD), Continuous stirred tank reactor (CSTR), Agaricus bisporus residue, Flow field

**Posted Date:** March 3rd, 2022

**DOI:** <https://doi.org/10.21203/rs.3.rs-1305350/v1>

**License:**  This work is licensed under a Creative Commons Attribution 4.0 International License.

[Read Full License](#)

---

# 1 Modelling of CSTR Flow Field for *Agaricus bisporus* Residue

## 2 Fermentation Based on CFD Numerical Simulation

3 Jiayu Li <sup>a</sup>, Jinping Zou <sup>a</sup>, Xuan Wei <sup>a,b\*</sup>

4 <sup>a</sup> College of Mechanical and Electronic Engineering, Fujian Agriculture and Forestry  
5 University, Fuzhou, Fujian, 350100, China; <sup>b</sup> College of Food Science, Fujian Agriculture  
6 and Forestry University, Fuzhou, Fujian, 350002, China

7 \* Corresponding author: Tel: +86 59183768192; E-mail: xuanweixuan@126.com

8 **Abstract:** *Agaricus bisporus* production gets a lot of residues, which could be fermented by a continuous  
9 stirred tank reactor (CSTR). This research was conducted to study the characteristics of the multiphase  
10 flow field in the reactor and its influence on the efficiency of biogas production in the CSTR  
11 fermentation process of *Agaricus bisporus* residue by using CFD numerical simulation technique. The  
12 aim is to reveal the relationship between the reactor operating conditions, flow field characteristics, and  
13 biogas production efficiency at the micro-level. We compared the results of different turbulence models  
14 by evaluating the power quotients and flow quotients with the experimental results to derive the most  
15 suitable flow field model inside the reactor for the *Agaricus bisporus* residues. The results showed that,  
16 under the condition that the number of grids does not affect the simulation results, and considering the  
17 model accuracy and efficiency, the numerical method can be chosen as the multiple reference frame  
18 (MRF) method of the second-order upwind discrete scheme with the realizable  $k - \varepsilon$  model. In this  
19 way, we can make use of edible mushroom residue as a substrate for resource utilization and provide  
20 basic data and theoretical basis for the design and scale-up with anaerobic fermentation to biogas reactor.

21 **Keywords:** Biogas; Computational fluid dynamics (CFD); Continuous stirred tank reactor (CSTR);  
22 *Agaricus bisporus* residue; Flow field

23

## 24 1. Introduction

25 Currently, agricultural residues are considered as a recycling resource. Appropriate treatment could make the  
26 residues to be energy resources and environmentally friendly (Bentsen et al. 2018). *Agaricus bisporus* residue is a  
27 mixture of residual fungus substrates and metabolites after *Agaricus bisporus* harvest (Cengiz et al. 2014). Due to  
28 the abundant nutrients in the residue, can be used as raw material for anaerobic fermentation to produce biogas.  
29 During anaerobic fermentation, complex polymers are transformed into biogas by methanogenic bacteria (Bedoya  
30 et al. 2020). Biogas is one of the most hopeful renewable energy sources nowadays, which has a great benefit both  
31 on environmental protection and energy-saving, especially in the treatment of organic waste (Moghtaderi et al.  
32 2006; Gronowska et al. 2009; Kumarappan et al. 2009; Esen & Yuksel 2013). A continuous stirred tank reactor  
33 (CSTR) is a widely used bioreactor in biogas engineering, which greatly increases the contact area between  
34 microorganisms and fermentation materials owing to the addition of a stirring device compared with other common  
35 reactors (Hassan et al. 2020).

36 In a fermentation reactor, mixing is an important operation to improve the efficiency of biogas anaerobic  
37 fermentation and biogas productivity by homogenizing the methanogenic bacteria, nutrients, and temperature  
38 throughout the reactor (Moretto et al. 2020; Villamil et al. 2020). Although modern biogas engineering generally  
39 incorporates mixing technology to improve fermentation efficiency (Leow et al. 2020), a large number of biogas  
40 projects use a simple mixing strategy, which doesn't help to enhance the efficiency of biogas production, and even  
41 consumes more energy (Luan et al. 2014). As the biogas anaerobic fermentation reactor needs to be sealed, it is  
42 hard to know the internal flow field of the reactor. So, the added mixing modules probably are not suitable for the  
43 reactor shape or the raw material characteristics, resulting in insufficient mixing (Munoz et al. 2018).

44 Computational fluid dynamics (CFD) modeling can accurately analyze the internal flow state of a biogas  
45 anaerobic reactor. It has been widely used in fluid mechanical process optimization to enhance biogas production  
46 by improving the mixing structure (Yang et al. 2012; Zou et al. 2012). The mixing process of fermentation fluid  
47 is essentially a flow process under the action of external forces, and CFD numerical simulation methods can help  
48 people understand its theoretical flow process and flow pattern (Wu 2013). In 2002, North Carolina State  
49 University firstly proposed how CFD can be used to investigate the fluid mixing flow patterns of biogas  
50 fermentation materials (Fleming & Graham 2002). Since then, many biogas fermentation reactor researchers  
51 have made significant progress based on the flow field patterns study. Some researchers have used CFD to visualize  
52 and analyze the flow pattern state formed during the mixing process (Mendoza et al. 2011), thus introducing

53 methods that can accurately verify and design mixing mechanisms (Ding et al. 2010; Bartzanas et al. 2013). These  
54 approaches made the internal mixing conditions in biogas fermentation reactors visualize and quantitative. For  
55 example, Luo (Luo et al. 2015) used CFD simulations to find that fermentation efficiency would be better in a  
56 long-cylinder anaerobic reactor if the stock was placed from the top and slowly settled by gravity in such a  
57 discharge. Marti-Herrero (Marti-Herrero et al. 2014) optimized the mixing flow pattern in the biogas reactor by  
58 improving the grid model, which resulted in a 44% increase in biogas production and the smooth operation of the  
59 reaction. Dapelo (Dapelo et al. 2015) applied the Euler-Lagrange model to a continuous stirred tank anaerobic  
60 fermentation reactor and modeled it using the CFD technique, which was found to be significant for studying the  
61 flow field changes inside the reactor. All these studies have shown that the material mixing process can be  
62 simulated by the CFD technique, which is an important technical approach to improve the mixing problem inside  
63 the reactor. It not only makes the study of mixing conditions inside biogas fermenters largely free from unseen  
64 conditions, but also promotes a level of scientific and accurate visualization and quantitative analysis of the  
65 research.

66 The objective of this paper is to study the fluid flow field characteristics on the efficiency of biogas  
67 production by CSTR using *Agaricus bisporus* residue as the substrate based on CFD numerical simulation  
68 technique. We hope to provide basic data of scale-up and design of anaerobic fermentation biogas reactor used the  
69 edible mushroom residue as substrate.

## 70 **2. Materials and methods**

### 71 ***2.1 Reactor geometry***

72 The tank and stirrer structure of the CSTR is shown in Figure 1. The shell of the tank is a traditional and  
73 economical circular tank with uniform force distribution. The addition of four vertical baffles can effectively  
74 weaken the tangential flow and enhance the axial and radial flow. The mixing mechanism of the reactor was  
75 designed as a double-layer paddle combination, with a four four-folded-blade open turbine paddle in the upper  
76 layer and a six-straight-blade disk turbine paddle in the lower layer, which was sealed by a shaft seal to the mixing  
77 shaft. The fermentation liquid of the *Agaricus bisporus* residue was filled to the hydrostatic level of  $H_L=360\text{mm}$ ,  
78 while the effective volume of the reactor was 28L. During mixing, the speed of the stirrer was 60 rpm, which was  
79 controlled by an adjustable speed device. There was a circulating water jacket on the outside of the reactor with a  
80 temperature control device to make the temperature stable.

81 **Fig 1.**

## 82 **2.2 Fluid dynamics governing equations**

83 The fluid flow in CSTR obeys the three conservation laws in fluid mechanics, which satisfied the  
84 momentum conservation equation, mass conservation equation, and energy conservation equation.

85 The mass conservation equation can be expressed as:

$$86 \quad \frac{\partial \rho}{\partial t} = \nabla \cdot (\rho \vec{v}) - S_m = 0 \quad (1)$$

87 the above equation refers to the mass of fluid flowing in per unit time is equal to the mass increased to per unit  
88 time, in this,  $\rho$  is the fluid density;  $t$  is the fluid flow time;  $\vec{v}$  is the velocity vector;  $S_m$  is the mass source  
89 term.

90 Momentum conservation can be expressed as:

$$91 \quad \frac{\partial(\rho u)}{\partial t} + \text{div}(\rho u \vec{u}) = -\frac{\partial P}{\partial x} + \text{div}(\mu \text{grad } u) + S_x \quad (2)$$

$$92 \quad \frac{\partial(\rho v)}{\partial t} + \text{div}(\rho v \vec{v}) = -\frac{\partial P}{\partial y} + \text{div}(\mu \text{grad } v) + S_y \quad (3)$$

$$93 \quad \frac{\partial(\rho w)}{\partial t} + \text{div}(\rho w \vec{w}) = -\frac{\partial P}{\partial z} + \text{div}(\mu \text{grad } w) + S_z \quad (4)$$

94 the change rate of momentum per unit time for the fluid is equal to the sum with volume force per unit volume in  
95 space, in equation,  $P$  is the pressure exerted on the micro-element body;  $u$ ,  $v$ ,  $w$  is the component of the three-  
96 dimensional velocity in the three directions;  $S_x$ ,  $S_y$ ,  $S_z$  is the volume force applied in the three directions.

97 The energy conservation equation can be expressed as:

$$98 \quad \frac{\partial(\rho T)}{\partial t} + \text{div}(\rho \vec{u} T) = \text{div}\left(\frac{k}{c_p} \text{grad } T\right) + S_T \quad (5)$$

99 assuming that the external force is only the volume force and area force, the change rate of kinetic energy and  
100 internal energy of the substance in the region  $\Omega$  is equal to the work done by the volume force and area force per  
101 unit time plus the heat given to the substance by the outside world per unit time, in the equation above,  $T$  is the  
102 temperature,  $c_p$  is the specific heat capacity,  $k$  is the heat transfer coefficient,  $S_T$  is the heat source of the fluid  
103 including the system itself and the energy converted from external energy.

104 In addition, the rheological equation is an equation that describes the relationship between fluid shear  
105 stress and fluid gradient for the mechanics to which the substance is subjected, of which the power law model is  
106 most commonly used and can be expressed as:

$$107 \quad \eta = K \dot{\gamma}^{n-1} \quad (6)$$

108 where  $\eta$  is viscosity,  $K$  is the consistency coefficient,  $\dot{\gamma}$  is the shear rate,  $n$  is the power law exponent.

109 This study mainly focused on the isothermal simulation of the internal flow of CSTR, and the heat transfer  
110 is not involved, so the law of energy conservation is not repeated.

### 111 **2.3 Definition of dimensionless number**

112 Since the fermentation fluid of *Agaricus bisporus* residue was an isothermal incompressible fluid at the  
113 fermentation temperature at 323.15 K and exhibits a non-Newtonian pseudo-plastic fluid behavior. Therefore, in  
114 the mechanically stirred reactor, the Reynolds number (Re) of the non-Newtonian fluid is expressed as (Chen  
115 1981):

$$116 \quad Re = \frac{\rho ND^2}{\eta} \quad (7)$$

117 where  $N$  is the rotating speed of the impeller,  $D$  is the diameter of the impeller, and  $\eta$  is determined by equation  
118 (6) in which the shear rate can be indicated as:

$$119 \quad \dot{\gamma} = K_s N \quad (8)$$

120 where  $K_s$  is a constant determined experimentally.

121 In a similar way to pipe flow, the Reynolds number of a fluid flowing through a moving zone can be  
122 expressed as:

$$123 \quad Re_g = \frac{\rho U_\infty^{2-n} d^n}{K(0.75 + \frac{0.25}{n})n 8^{n-1}} \quad (9)$$

124 where  $U_\infty$  is the average velocity of the fluid at the exit of the moving zone, and  $d$  is the diameter of the moving  
125 zone.

126 The power quotient ( $N_p$ ) and the flow quotient ( $N_Q$ ) in the mixing vessel are expressed as (Paul et al.  
127 2004):

$$128 \quad N_p = \frac{P}{\rho N^3 D^5} \quad (10)$$

$$129 \quad N_Q = \frac{Q}{ND^3} \quad (11)$$

130 where  $P$  is the power input, and  $Q$  is the flow rate through the moving zone.

### 131 **2.4 Mathematical models and solution methods**

132 The CFD preprocessing software GAMBIT and the commercial CFD package Fluent 2020R1 (ANSYS-  
133 Fluent, Inc., 2020) were used in this study. CFD modeling includes preprocessing, model setup, iterative

134 calculations, and post-processing of the results. Both the baffle and impeller blades were treated as zero-thickness  
135 walls in the preprocessing to reduce the number of meshes. The multiple reference frame (MRF) was used in this  
136 study to deal with the rotation in the stirrer region. MRF is a steady-state approximation method but gives good  
137 simulation results in non-steady-state problems. The whole CSTR computational domain is decomposed into  
138 several subdomains, i.e., rotational domain and stationary domain with different reference systems set for each  
139 subdomain in the MRF. The shaft and the paddle of the stirrer were moving boundaries, and when the stirrer was  
140 in the rotational domain, the motion has the same speed as the fluid in this subdomain; when the stirrer was in the  
141 stationary domain, it was moving compared to the fluid in this subdomain. The stirrer subdomain in the reactor  
142 adopted the non-inertial coordinate system with synchronous rotation to the stirring shaft, while the inertial  
143 coordinate system was used in the stationary domain of the reactor besides the stirrer.

## 144 ***2.5 Boundary conditions and initial conditions***

145 In this study, the flow field was numerically simulated for the fermentation fluid of *Agaricus bisporus*  
146 residue in CSTR, where the material was characterized as a gas-liquid-solid three-phase fluid with small solid  
147 particles. Some research (Hooshyar et al. 2013) results showed that when the solid phase particle diameter at 0.078-  
148 0.587mm, there was no collision effect between solid particles and bubbles, and they followed the main fluid  
149 movement; when the particle diameter was 2.0-4.0mm, the particles were not easily followed by the liquid phase  
150 flow, the solid phase and gas phase had obvious collision occurring at this time, which would make the bubbles  
151 occurred deformation effect and impact the movement speed of bubbles. Due to the *Agaricus bisporus* residue  
152 after being crushed and sieved, the obtained particles were less than 0.5 mm. According to the above study, the  
153 effect between particles and bubbles can be ignored, therefore it can be considered as a gas-liquid two-phase  
154 system.

155 With the selection of double-precision and the 3D model in Fluent software, the boundary conditions and  
156 initial conditions were set as follows:

157 1. Selected the pressure-based solver, and the time was set to transient mode, and the gravitational  
158 acceleration in Z direction was set to  $-9.81m/s^2$ .

159 2. Since the medium in CSTR was biogas and *Agaricus bisporus* residue fermentation broth, the  
160 multiphase flow model was adopted as methane and water, where the density and viscosity of water were changed  
161 to the value of *Agaricus bisporus* residue fermentation broth to simulate its slurry phase. The multiphase flow

162 models in Fluent are powerful in the calculation, including the volume of fluid (VOF) model, the mixture model  
163 and the Eulerian model, and different multiphase flow models are used for different flow forms. Therefore, it is  
164 necessary to choose a suitable multiphase flow model for the material characteristics of this study, and because we  
165 mainly investigated the flow field distribution patterns of gas-liquid two phases, the Eulerian model was finally  
166 chosen.

167 3. The fluid flow in bioreactor mainly includes laminar flow and turbulent flow, in which turbulence is  
168 more common and its flow is more complicated. When using CFD to deal with turbulence problems, an appropriate  
169 model is crucial to characterize the flow field (Wu 2011). Turbulence models are generally classified into three  
170 types: Reynolds-averaged Navier-Stokes (RANS) models, large eddy simulation (LES) models, and direct  
171 numerical simulation (DNS) models. Among them, the RANS model is less computationally intensive and can  
172 simulate basically all fluid turbulent motions. For this feature, this study mainly focused on the subordinate model  
173 in the RANS turbulence model for simulation analysis.

174 The RANS model, which averages the transient turbulent flow in time by using the Navier-Stokes  
175 equation, is characterized by its less amount of computation and its ability to simulate almost all fluid turbulent  
176 motions. The RANS model contains a series of affiliated models: such as the  $k$ -epsilon model, the  $k$ -omega model,  
177 the Reynolds-Stress model, etc. Compared with the RANS model, the LES model is only used for larger-scale  
178 vortices by filtering functions, which require more computation meshes and computational amount. Without  
179 making any turbulence assumptions and solving the transient Navier-Stokes equation directly, the DNS model has  
180 the advantage that all turbulence characteristics can be calculated but cost much. Therefore, in comparison, the  
181 most economical and efficient turbulence model is RANS for this study.

182 The turbulence model in this study was based on the RANS model, which included one-equation ( $k$ ),  
183 two-equation ( $k - \epsilon$  or  $k - \omega$ ), the RSM, etc. Some researchers used a low-Reynolds-number  $k - \epsilon$  model to  
184 simulate the anaerobic digestion mixing process, and it was found that the computational cost is high even though  
185 it is superior to the other two-equation models (Wu 2010). Meanwhile, the researchers pointed out that the standard  
186  $k - \omega$  and realizable  $k - \epsilon$  models can be used as recommendations in mechanical mixing of non-Newtonian  
187 fluids (Wu 2011). The fluid in the CSTR was powered by the stirrer and its flow was turbulent. Since the stirrer  
188 rotates faster than the slight rotation, the standard  $k - \omega$  model with shear flow correction, the realizable  $k - \epsilon$   
189 model and the RSM (Reynold stress model) were used in this study for computational simulation to compare the  
190 applicability of the three models. Table 1 shows the general scope of application and advantages of the three RANS  
191 models.

192 **Tab 1.**

193 4. The boundary conditions were set to pressure inlet, only the gas entry was considered, the volume  
194 fraction of methane was set to 1, the top outlet allowed only the gas phase to flow out, and the side outlet was set  
195 as the wall. The reactor shell, stirrer, and shaft were also set as the wall, and the rotational coordinates and rotational  
196 speed of the stirrer and shaft were set separately to distinguish the relative and absolute velocities between them.

### 197 **3. Results and discussion**

198 In a mixing and stirring reactor, the power number of the impeller is similar to the friction coefficient in  
199 a pipe flow, or the drag coefficient of a solid object immersed in the flow. While the power number is inversely  
200 proportional to the Reynolds number when the fluid is in laminar flow, it is constant and independent of the  
201 Reynolds number in a turbulent flow. The turbulence model tests in this study were conducted in an elliptical  
202 bottom cylindrical reactor as shown in Figure 1, with four uniformly distributed baffles and a double layer stirrer  
203 arranged inside. The mixing unit consisted of a four-folded-blade open turbine paddle and a six-straight-blade disk  
204 turbine paddle, as shown in Figure 2. And the fluid inside the reactor is a non-Newtonian fluid, then in the  
205 experiment, the power quotient and flow quotient of the impeller were 0.77 and 0.39 respectively. To quantitatively  
206 evaluate the performance of the turbulence model, three error indicators were proposed:

$$207 \quad \delta_P = \left| \frac{N_P - N_{P,lab}}{N_{P,lab}} \right| \times 100\% \quad (12)$$

$$208 \quad \delta_Q = \left| \frac{N_Q - N_{Q,lab}}{N_{Q,lab}} \right| \times 100\% \quad (13)$$

$$209 \quad \delta = 0.5(\delta_P + \delta_Q) \quad (14)$$

210 where  $\delta_P$  and  $\delta_Q$  are errors for predicted power and flow numbers,  $N_{P,lab}$  and  $N_{Q,lab}$  are obtained from the  
211 lab specifications, and  $\delta$  is the weighted mean error.

212 **Fig 2.**

#### 213 **3.1 Grid model assessment**

214 The quantity and quality of the mesh directly affect the accuracy of the computational results. When the  
215 mesh quantity is too small, the model cannot have a reasonable mesh assignment, which makes the whole mesh  
216 quality low, so the computational accuracy is seriously reduced, and the computation will not be carried out  
217 smoothly. And when the number of meshes is too large, it will require higher computer configuration, making the

218 computational time longer and reducing the work efficiency significantly. To determine the effect of mesh quantity  
219 on the simulation results in the CSTR, this study used six sets of meshes for computations with the mesh division  
220 numbers of 248936, 485423, 603584, 875067, 1248962, and 1756961. In addition, the turbulent kinetic energy and  
221 turbulence intensity of the six mesh models were compared as shown in Figure 3.

222 **Fig 3.**

223 The figure illustrates the variation of turbulent kinetic energy as well as turbulent intensity with the change  
224 of mesh number. When the mesh number is from 240,000 to 870,000, the turbulent kinetic energy and turbulent  
225 intensity decrease sharply; and then they are level off gradually when the mesh number is from 880,000  
226 to 1,800,000. So, it can be seen that the influence on the numerical analysis results is not obvious when the mesh  
227 number is more than 800,000. Considering the mesh quality, computational accuracy, computational volume, and  
228 computer configuration requirements, this study selected the mesh number of 875067 for the CFD simulation of  
229 CSTR.

230 In order to further assess the independence of the meshes, the numerical simulation results were compared  
231 with 603584, 875067, and 1248962 grid numbers respectively. Due to the symmetry of the constructed CSTR  
232 model, the velocity distribution on this cross-section during the stirring paddle operation also has symmetrical  
233 characteristics. In this study, we took the cross-section 180 mm above the origin of the CSTR model and compared  
234 the velocity variation on this cross-section, and used the velocity of this cross-section on the radius of the X-Y  
235 plane as the object of analysis, as shown in Figure 4.

236 **Fig 4.**

237 From Fig. 4, it can be seen that the maximum relative error between mesh numbers 875067 and 1248962  
238 is 3.33%, which is smaller than the maximum relative error between mesh numbers 603584 and 875067, which is  
239 8.54%, so we concluded that continuing to increase the number of meshes would no longer improve the  
240 computational accuracy significantly, and the mesh size can already reach the computational accuracy requirement.  
241 Furthermore, using a large number of meshes does not improve the prediction of the model because it produces a  
242 high discretization error. Therefore, the CSTR model with a mesh number of 875067 was adopted for further  
243 simulation.

244 **3.2 Evaluation of turbulence models**

245 Considering that the *Agaricus bisporus* residue exhibits incompressible non-Newtonian fluid properties

246 when the temperature is 323.15 K and the inoculum concentration is 50%, and the rheological properties are similar  
247 to water, the Reynolds number can be determined by equations (7) and (8) when the impeller speed  $N = 60$  rpm,  
248 which yields  $Re = 3710$ , and Table 2 shows the Reynolds number values under different turbulent flow models.  
249 Based on the input of these parameters, three turbulence models were used for the numerical simulation of the  
250 *Agaricus bisporus* residue fluid within the CSTR. Table 3 shows the power quotients and flow quotients predicted  
251 by equations (10) and (11), where the torque and pumping capacity of each simulated impeller were obtained by  
252 post-processing. The results illustrate that the performance is better in predicting the flow quotients than the power  
253 quotients in CFD numerical simulations, and the realizable  $k - \varepsilon$  model can be realized with the highest accuracy  
254 in the prediction results of the power quotient and flow quotient, and the standard  $k - \omega$  model has higher  
255 accuracy in the prediction of the power quotient than the RSM model, while the prediction accuracy of the flow  
256 quotient is lower than that of the RSM model.

257 **Tab 2.**

258 **Tab 3.**

259 Table 3 also shows the weighted mean error values in the three turbulence models, where equal weights  
260 are assumed for the power quotient and the flow quotient. If the errors are generated during numerical  
261 computations and experiments, this turbulence model can be considered as having excellent prediction results  
262 when  $\delta \leq 10\%$ . However, because there is no quantitative criterion for evaluating the turbulence model, and  
263 considering the efficiency of the calculation as well as the economy, we can set the error standard value  $\delta \leq 30\%$ ,  
264 the prediction results of the turbulence model are applicable. Combining the error analysis and the convergence  
265 results of each run, we found that all three turbulence models were able to predict the mechanical stirring of the  
266 *Agaricus bisporus* residue fluid within the CSTR at an operating condition of 323.15 K, with appropriate CPU  
267 operation time and high stability. Among them, the realizable  $k - \varepsilon$  model performs slightly better than the other  
268 two models, the standard  $k - \omega$  model converges relatively fast, and the RSM has the highest computational cost.  
269 Consequently, in the flow of mechanical stirring, it is recommendable to use the realizable  $k - \varepsilon$  model and  
270 switch to the RSM if needed.

### 271 ***3.3 Changes in the flow pattern of the fluid field***

272 When simulating the flow pattern of a flow field, in general, based on the empirical value of  $K_s$ , the  
273 Reynolds number of a non-Newtonian fluid during mechanical stirring can be calculated by equations (7) and (8)

274 to determine the flow regime (laminar, transition or turbulent). For some commonly used impellers, the  
275 experimental data of  $K_s$  in have been much studied. However, if  $K_s$  is unknown for the impeller, the flow  
276 information of the moving zone can be used to calculate the Reynolds number ( $Re_g$ ) defined by equation (9). As  
277 Table 2 shows the  $Re$  and  $Re_g$  values in different turbulence model calculations, it can be seen that the  
278 differences are not significant. Therefore, when the  $K_s$  is unknown, the  $Re_g$  value calculated from the moving  
279 zone is an acceptable value within the error range. In this study, as  $K_s$  was unknown, the simulation analysis was  
280 based on using  $Re_g$  values.

281 After obtaining the converged flow field, the flow pattern within the CSTR can be visualized. Take  $N=60$   
282 rpm as an example, Figure 5 shows the global velocity vector diagram in the vertical plane in the middle of the  
283 four baffles, which is the flow field characteristic of the two impellers during anaerobic fermentation. When the  
284 impellers start to rotate, due to the double-layer paddles of the reactor, the impeller blades drove the fermentation  
285 broth downward to the bottom of the vessel. Meanwhile, the fermentation broth flow radially toward the sidewalls  
286 of the reactor when it has undergone radial diffusion and separately flow upward and downward along the walls.  
287 So, the fermentation broth would form a larger circulation near the upper four-fold blades and two smaller  
288 circulations near the lower six-straight-blade disk turbine paddle before returning axially to the upper part of the  
289 double-layer impeller. As shown in figure 5, the contour bars represent the velocity scale from zero (blue area) to  
290 the maximum value (red area), where the velocity amplitude is greater than (or equal to) the specified maximum  
291 value. This method was applied to all the visualized flow field contour plots in this study.

292 **Fig 5.**

### 293 ***3.4 Impact of discrete schemes***

294 For the partial derivative equations established in the solution domain, there are theoretically exact  
295 solutions, but due to the complexity of the fluid flow problems dealt with, it is generally difficult to obtain exact  
296 solutions to the equations. Therefore, it is necessary to treat the dependent variables at a finite number of locations  
297 (grid nodes or grid centroids) in the computational domain as fundamental unknowns by numerical methods, so  
298 as to build a set of algebraic equations about these location quantities, and then obtain these node values by solving  
299 the set of algebraic equations, while the values at other locations in the computational domain are determined  
300 according to the values at the node locations. In this way is how the discrete equations were established, while the  
301 discrete scheme is also called interpolation method, as shown in Table 4 for the discrete scheme types utilized in

302 this study.

303 **Tab 4.**

304 **Tab 5.**

305 To investigate the effect of the discrete equations on the power quotients and flow quotients, the  
306 momentum equation was set to the second-order upwind differential discrete equation, and the other settings were  
307 kept constant. To save computational time, the iterations started from the first-order upwind differencing discrete  
308 equation, and then switched to the second-order discrete equation. Numerical simulations were performed for the  
309 three types of turbulence models separately, as the results in Table 5 show that the power quotient of the standard  
310  $k - \omega$  model decreases from 0.67 to 0.66, with a 1.3% increase in its error value, while the flow quotient improves  
311 significantly, from 0.32 to 0.36, with a 10.3% decrease in its error value. For the realizable  $k - \varepsilon$  model, the  
312 power quotient drops from 0.70 to 0.69 and its error value increases by 1.3%, and the flow quotient raises from  
313 0.37 to 0.38, and its error value reduces by 2.5%. Besides, the power quotient of the RSM model decreases from  
314 0.65 to 0.63 and its error value increases by 2.6%, but the flow quotient increases from 0.35 to 0.37, and its error  
315 value decreases by 5.2%. In summary, the simulation analysis using the second-order upwind discrete format has  
316 improved the accuracy of its predicted flow quotients, however, the accuracy of the power quotients has decreased.  
317 Consequently, if the flow collimator is the main parameter of interest, the second-order upwind differencing  
318 discrete equation can be used.

### 319 ***3.5 Impact of numerical methods***

320 When the stirring mechanism in a reactor rotates, fluid separation with vortex generation occurs behind  
321 its impeller, and the vortex is transmitted to the flow body through convective and turbulent flow, and the flow  
322 field motion appears periodic. As a result, a key issue in the CFD numerical simulation of stirred reactors is the  
323 simulation of impeller rotation and the resolution of the interaction between the moving impeller and the stationary  
324 baffle. The commonly used numerical simulation methods are the impeller boundary condition method, the  
325 momentum source-sink method, the inner-outer iterative procedure method, the multiple reference frame (MRF)  
326 method, and the sliding-grid method, as shown in Table 6 for the definition of the two numerical methods used in  
327 this study their characteristics.

328 **Tab 6.**

329 **Tab 7.**

330 In this study, to investigate the effect of numerical methods on the power and flow quotients, simulations  
331 were built based on the convergence of the flow field by the MRF method and then by the Sliding-grid method.  
332 This modeling strategy requires switching the conformal interface between the moving and stationary regions to a  
333 non-conformal interface. As the Sliding-grid method solves the transient flow field problem, the grid around the  
334 stirred impeller is physically shifted during the solution process. Typically, the impeller torque versus time shows  
335 a sinusoidal curve with a periodicity, where the highest value occurs at the moment when the blade tip reaches the  
336 baffle, and the lowest value occurs when the blade tip reaches the midpoint of the two baffles. The torque on the  
337 highest value was taken to calculate the power quotient, as the four-blade tips were set to face the four baffles in  
338 the pre-processing of Gambit. Table 7 shows the power quotients and flow quotients predicted by the Sliding-grid  
339 method with the grid model setting unchanged. Combing with Table 3 for the MRF method, it can be seen that the  
340  $N_p$  value of the standard  $k - \omega$  model rises from 0.67 to 0.69, with a  $\delta_p$  reduction of 2.6%, and the  $N_Q$  value  
341 rises from 0.32 to 0.34, with a  $\delta_Q$  reduction of 5.2%. The  $N_p$  value obtained from the realizable  $k - \varepsilon$  model  
342 increases from 0.70 to 0.73, with  $\delta_p$  decreasing by 3.9%, and the  $N_Q$  value remains unchanged. The RSM model  
343 predicted the  $N_p$  value to increase from 0.65 to 0.67 with a 2.6% decrease in its  $\delta_p$ , while there is no change in  
344 the  $N_Q$  value. The summary of the above, compared with the MRF method, the Sliding-grid method improves the  
345 prediction results overall, but it requires longer CPU time to obtain a solution. From an engineering point of view,  
346 the MRF method is recommended because its accuracy is within the acceptable range and its computational cost  
347 is low.

### 348 **3.6 Model Validation**

349 Model validation was carried out in the laboratory of the Department of Agricultural Engineering, Fujian  
350 Agriculture and Forestry University. During the experiment, 25% inoculum concentration of *Agaricus bisporus*  
351 residue was mechanically stirred in a CSTR with an elliptical-bottomed cylindrical reactor shape with four internal  
352 baffles, equipped with a four-folded-blade open turbine paddle and a six-straight-blade disk turbine paddle (D=86  
353 mm). The fermentation temperature was maintained at 323.15 K and the impeller was operated in N=60 rpm mode  
354 measured by a sensor. Due to the uniqueness of the two-paddle structure and the rheological properties of the  
355 *Agaricus bisporus* residue, the CFD numerical simulations were simplified for the reactor and simulated *Agaricus*  
356 *bisporus* residue properties similar to water. Figure 6 shows the comparison of simulated and measured axial  
357 velocities with the radial position at  $z = 180$  mm. The CFD predictions are in reasonable agreement with the

358 measurements when impeller replacement, the use of rheological property approximations, measurement  
359 inaccuracies, and numerical errors are taken into account. It shows that the prediction results of realizable  $k - \varepsilon$   
360 model among the three types of models is closer to the experimental values. In addition, when using the grid  
361 number of 875067, the discretization scheme of first-order upwind format, and the numerical simulation method  
362 of MRF method, the weighted average errors are within 30% of both of the power quotients and flow quotients of  
363 the predicted models (Table 8), indicating that the simulation results are acceptable.

364 **Fig 6.**

365 **Tab 8.**

## 366 **4. CFD visualization of the impeller blade**

### 367 ***4.1 Velocity cloud plot of longitudinal section distribution***

368 The velocity cloud plot is used to represent the different velocities in different colors after the CFD  
369 simulation calculation, so it can visually describe the velocity distribution in each region of the reactor. Since the  
370 baffles can change the fluid flow pattern developed by the stirring paddles, the plane directly perpendicular  
371 between two baffles was selected as the cutting surface for observation. Figure 7 shows the velocity distribution  
372 cloud in the longitudinal section, it can be seen that the maximum velocity of each paddle is located at the end of  
373 each paddle, and it can be clearly observed that the fluid velocity in the rotation region of each paddle decreases  
374 in a gradient from the paddle area to the wall direction.

375 **Fig 7.**

376 There is a velocity dead zone below the lower six-straight-blade disk turbine paddle, where the mixing  
377 and transfer of material take place mainly by free diffusion. The formation of the bottom stirring dead zone may  
378 be the result of flow field circulation and gas-liquid two-phase interaction. It also can be seen that the bottom of  
379 the reactor has some radial flow, the disturbance from the stirring paddles develops below the top surface of the  
380 upper paddles rather than throughout the reactor. This not only has no influence on the adequate mixing of fluids  
381 in the paddling zone, but also provide a stable flow field environment for microbial growth and metabolism.

### 382 ***4.2 Velocity cloud plot of cross section distribution***

383 The impeller blades are the power source of all fluid flow in the reactor, and the fluid flow in the impeller

384 zone largely determines the mixing of the fermentation broth in the whole reactor. Therefore, studying the velocity  
385 distribution of the fluid in the paddling zone helps us to have a comprehensive understanding of the role of the  
386 stirring paddle. In this paper, the cross-section of the paddles was selected as the object of study, and the center  
387 planes of the upper and lower paddles were analyzed separately to obtain the visualization cloud diagram of the  
388 stirring paddle combination as shown in Figure 8. The figure shows that the liquid near the baffle became turbulent  
389 due to the action of the baffle, and a small vortex appears behind the baffle, which effectively prevents the  
390 formation of large vortices throughout the reactor.

391 **Fig 8.**

392 The tangential flow generated by the rotation is transformed into radial and axial flow by the baffle, which  
393 increases the shear strength of the fluid and thus improves the mixing efficiency. In this way, the baffle can improve  
394 the circulation of the main body, increase the mixing efficiency in the reactor, and make the stirring result more  
395 desirable. In addition, we can clearly observe from it that the peak velocity is distributed in the paddle end region  
396 and spread around the reactor. An axial motion is generated near the four-folded-blade open turbine paddle, and  
397 the blade inclination lead to an oblique upward motion of the paddle wake, which folds when it hits the reactor  
398 wall and the reactor bottom, forming an axial circulation loop, and the paddle action cannot reach the top of the  
399 mixing tank, and these findings are consistent with the velocity vector plot observations. In the lower six- straight-  
400 bladed disk turbine paddle velocity cloud diagram, it can be seen that the flow field perturbation are more intense  
401 and the perturbation spreads outward from the tip of the stirring paddle and folds back after hitting the inner wall  
402 of the reactor, thus forming a complete circulation.

403 **5. Conclusion**

404 By comparing the power quotients and flow quotients of the three types of turbulence models under  
405 different conditions, it is found that the realizable  $k - \varepsilon$  model has the best performance. When a non-Newtonian  
406 fluid moves in a stirring machine, the value of  $K_s$  is an agnostic quantity, then the flow state can be judged by the  
407 Reynolds number calculated from the moving region and then conservatively valued. In choosing the discretization  
408 scheme, when the momentum conservation equation was set to the second-order upwind discretization, the  
409 predicted flow quotients were more accurate, but the accuracy of the power quotients decreased. Among the effects  
410 of numerical methods on model results, the comparison of predicted and experimental values showed that the  
411 Sliding-grid method was more accurate than the MRF method in predicting power quotients and flow quotients,

412 but with the consideration of computationally intensive and computation time, it is more efficient to use the MRF  
413 method in practice. In summary, in the anaerobic fermentation CSTR of *Agaricus bisporus* residues, the standard  
414  $k - \omega$  model with a first-order upwind discretization scheme and MRF method can be used when the accuracy  
415 demand is low, and the computation time is required to be fast. When a certain accuracy is guaranteed and the  
416 calculation time is appropriate, the second-order upwind discretization format with MRF numerical method can  
417 be altered as the realizable  $k - \varepsilon$  model. The RSM model with a combination of the second-order upwind  
418 discretization format and the Sliding-grid method can be used when the accuracy requirement is higher.

419

420

421 **Appendix:**

422 **Tab 1.** Advantages and disadvantages of three RANS models and applications.

<b>Model Category</b>	<b>Features and application occasions</b>
<b>Realizable k-epsilon</b>	Suitable for complex shear flows involving rapid strain, slight rotation, vortices, and local transition flows (e.g., delimited layer separation, large-scale separation, and obtuse body wake vortex shedding, large-angle diffuser stall, indoor ventilation, etc.).
<b>RNG k-epsilon</b>	Most of the advantages are similar to Realizable k-epsilon but harder to converge than it. Suitable for strong rotation cases (e.g., rotating machinery).
<b>RSM</b>	The most physically sound RANS model with the isotropic vortex viscosity assumption was removed. Higher requirements for computer CPU and the high coupling strength between equations, thus more difficult to converge. Suitable for complex 3D flows involving strong streamline curvature and strong rotation (e.g., curved pipes, rotating flow channels, rotating combustors, cyclones, etc.).

423 **Tab 2.** Reynolds number for different turbulence models.

<b>Turbulence model types</b>	<b>Reg</b>	<b>Error [%]</b>
<b>Standard k-<math>\omega</math></b>	3867	4.2
<b>Realizable k-<math>\epsilon</math></b>	3740	0.8
<b>RSM</b>	3525	5.0

424 Note: Temperature=323.15 K; Inoculum Concentration=50%; N=60 rpm; Re=3710.

425 The error calculations were based on the Reynolds number obtained from equation (7).

426 **Tab 3.** Power quotients and flow quotients for different turbulence models.

<b>Turbulence model types</b>	<b><math>N_p</math></b>	<b><math>\delta_p</math>[%]</b>	<b><math>N_Q</math></b>	<b><math>\delta_Q</math>[%]</b>	<b><math>\delta</math>[%]</b>
<b>Standard k-<math>\omega</math></b>	0.67	13.0	0.32	18.0	15.5
<b>Realizable k-<math>\epsilon</math></b>	0.70	9.1	0.37	5.1	7.1
<b>RSM</b>	0.65	15.6	0.35	10.3	13.0

427 **Tab 4.** The discrete scheme types utilized in this study.

Discrete scheme type	Definitions and characteristics
<b>First-order upwind scheme</b>	It means that the unknown quantity on the interface takes the value of the upstream node constantly. It does not cause any oscillation of the solution under any calculation conditions and is stable. However, when $Pe$ is large, the pseudo-diffusion is serious, and it is often necessary to encrypt the grid.
<b>Second-order upwind scheme</b>	The second-order upwind format is similar to the first-order upwind format in that both determine the physical quantities controlling the volume interface from the physical quantities of the upstream cell nodes. However, the second-order format uses not only the value of the nearest upstream node but also the value of another upstream node.

428 Note:  $Pe$  represents the ratio of ‘convection/diffusion’ intensity.

429 **Tab 5.** Power quotients and flow quotients under the influence of discrete schemes.

Turbulence model types	$N_P$	$\delta_P$ [%]	$N_Q$	$\delta_Q$ [%]
<b>Standard k-<math>\omega</math></b>	0.66	14.3	0.36	7.7
<b>Realizable k-<math>\epsilon</math></b>	0.69	10.4	0.38	2.6
<b>RSM</b>	0.63	18.2	0.37	5.1

430 **Tab 6.** Definition and characteristics of the numerical simulation methods used in this study.

Numerical simulation methods	Definition and Characteristics
<b>Multiple Reference Frame (MRF)</b>	This is a steady-state calculation method in which the rotational coordinates are used as the reference system in the cylindrical stirring region, while the fixed coordinates are used as the reference system in the rest of the region, and the coupling of the rotational coordinate system region with the fixed coordinate system region is done through the boundary conditions of various physical scalars. The advantage is that the overall numerical simulation of the flow field in the stirred reactor is achieved, and experimental assistance is no longer required.

**Sliding-grid Method**

This is a non-stationary calculation method, which is suitable for the prediction of the strong interaction regime of paddles and baffles, as well as for the study of some transient flow details of the start-up or periodic processes. The biggest drawback of this method is that the calculation requires a lot of time and a more complicated post-processing process.

431 **Tab 7.** Power quotient and flow quotient after changing the numerical simulation method.

<b>Turbulence model types</b>	$N_p$	$\delta_p$ [%]	$N_q$	$\delta_q$ [%]
<b>Standard k-<math>\omega</math></b>	0.69	10.4	0.34	12.8
<b>Realizable k-<math>\epsilon</math></b>	0.73	5.2	0.37	5.1
<b>RSM</b>	0.67	13.0	0.35	10.3

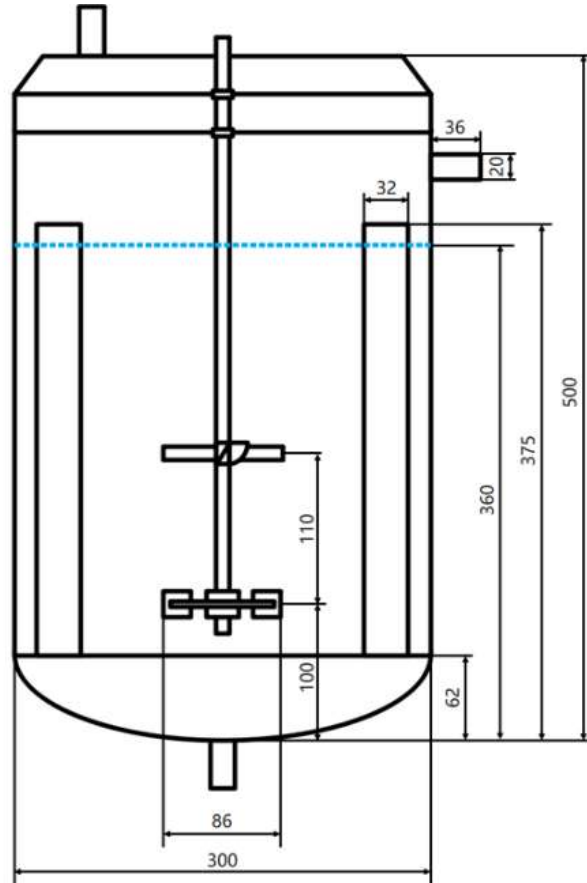
432 **Tab 8.** Weighted mean error values for different model schemes.

<b>Turbulence model types</b>	<b>First-order upwind method + MRF method</b>	<b>Second-order upwind method + MRF method</b>	<b>First-order upwind method + Sliding-grid method</b>
	$\delta$ [%]	$\delta$ [%]	$\delta$ [%]
<b>Standard k-<math>\omega</math></b>	15.5	11.0	11.6
<b>Realizable k-<math>\epsilon</math></b>	7.1	6.5	5.2
<b>RSM</b>	13.0	11.7	11.7

433

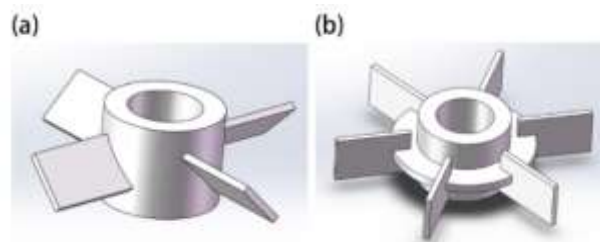
434

435 **Fig 1.** The geometry of the reactor for biogas production from *Agaricus bisporus* residue with  
436 dimensions in mm. The reactor was equipped with 2 turbine paddles and 4 baffles. During  
437 anaerobic fermentation, the reactor has a liquid static height of 360mm.



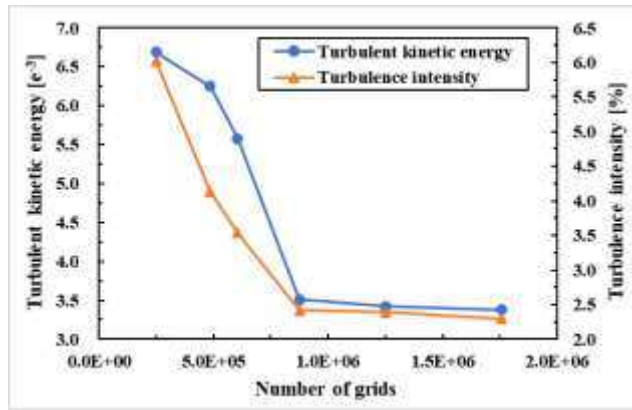
438

439 **Fig 2.** Two impellers for CFD simulation. Note:(a): the four-folded-blade open turbine  
440 paddle; (b): the six-straight-blade disk turbine paddle.



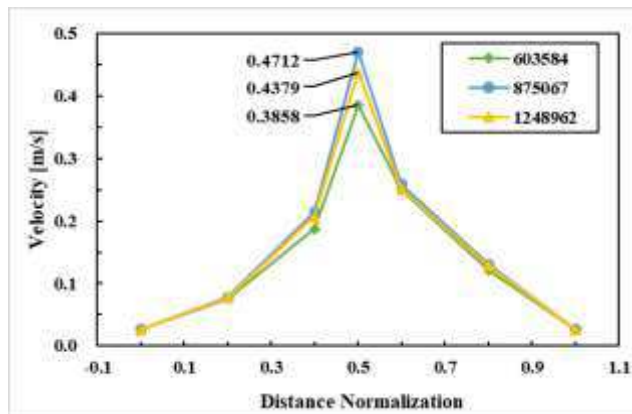
441

442 **Fig 3.** Variation curves of turbulent kinetic energy and turbulent intensity for different grid  
443 numbers.



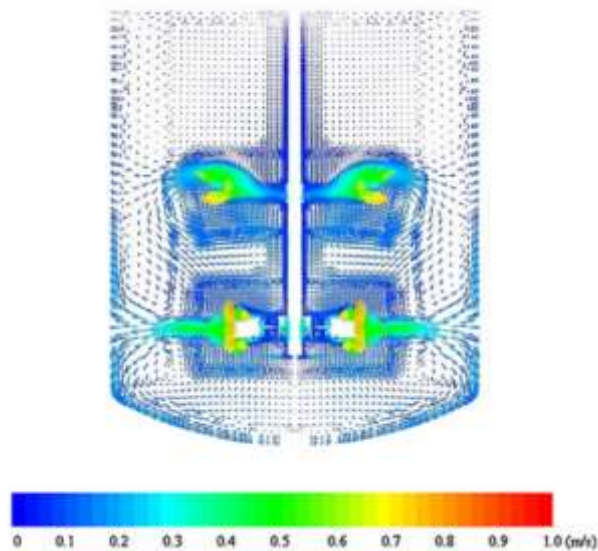
444

445 **Fig 4.** Variation curve of velocity with distance for different grid numbers.



446

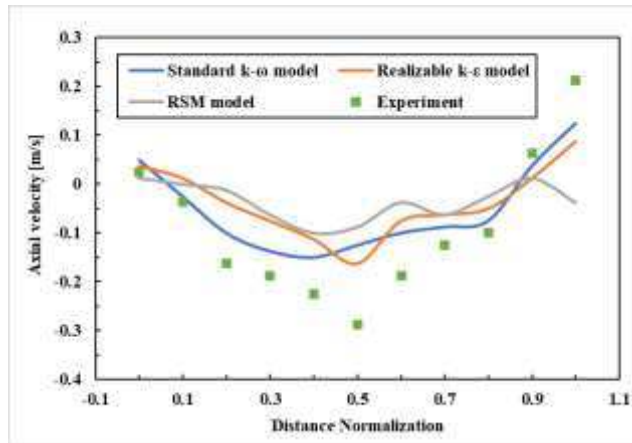
447 **Fig 5.** Global velocity vectors in the vertical plane inside the reactor.



448

449 **Fig 6.** Comparison of CFD simulation results of axial velocity in different turbulence models

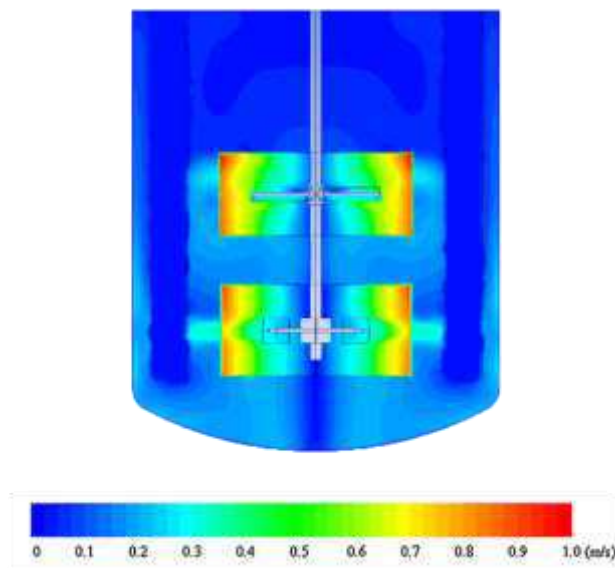
450 with experimental values.



451

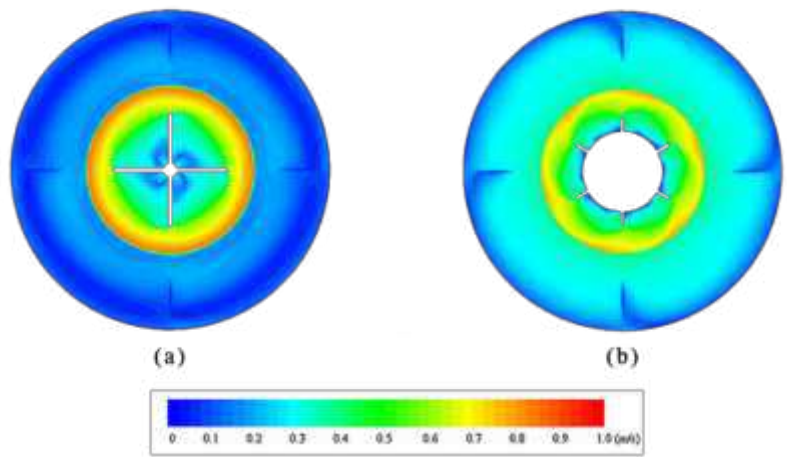
452 Note: Where a positive value means the velocity direction is vertically upward along the axis and a  
 453 negative value means the velocity direction is vertically downward along the axis.

454 **Fig 7.** CSTR internal longitudinal section velocity distribution cloud diagram.



455

456 **Fig 8.** Cloud diagram of velocity distribution in the center cross-section of two layers of  
 457 paddles.



458

459 Note: (a) represents the upper four-folded-blade open turbine paddle; (b) represents the lower six-  
460 straight-blade disk turbine paddle.

461

462 **Acknowledgements**

463 The authors gratefully acknowledge the financial support provided by the National Natural Science Foundation of  
464 China (No. 61705037). The authors also thank the project of Gaoyuan Agricultural Engineering of Fujian  
465 (712018014).

466 **Author information**

467 **Affiliations:**

468 College of Mechanical and Electronic Engineering, Fujian Agriculture and Forestry University, Cangshan District,  
469 Fuzhou City, Fujian Province, China

470 Jiayu Li, Jinping Zou, Xuan Wei

471 College of Food Science, Fujian Agriculture and Forestry University, Cangshan District, Fuzhou City, Fujian  
472 Province, China

473 Xuan Wei

474 **Contributions:**

475 Xuan Wei formulated the research questions and identified the research ideas. Jinping Zou provides test material.

476 Jiayu Li completed the theoretical and empirical analysis, and was a major contributor in writing the manuscript.

477 All authors read and approved the final manuscript.

478 **Corresponding author:**

479 Xuan Wei.

480 **Ethical Declarations**

481 **Competing interests:** The authors declare that they have no conflict of interest.

482 **Ethical approval:** Human and Animal Rights Not applicable.

483 **Consent to Participate:** Not applicable.

484 **Consent to Publish:** Not applicable.

485 **Availability of data and materials:** The datasets used or analyzed during the current study are available from the  
486 corresponding author on reasonable request.

487

## References:

488

- 489 Bartzanas T, DD Bochtis, O Green, CG S Rensen & D Fidaros (2013) Prediction of quality parameters for  
490 biomass silage: A CFD approach. *Computers & Electronics in Agriculture* 93:209-216.
- 491 Bedoya K, O Hoyos, E Zurek, F Cabarcas & JF Alzate (2020) Annual microbial community dynamics in a full-  
492 scale anaerobic sludge from a wastewater treatment in Colombia. *SCI TOTAL ENVIRON* 726.  
493 <https://doi.org/10.1016/j.scitotenv.2020.138479>
- 494 Bentsen NS, D Nilsson & S Larsen (2018) Agricultural residues for energy - A case study on the influence of  
495 resource availability, economy and policy on the use of straw for energy in Denmark and Sweden. *BIOMASS*  
496 *BIOENERG* 108:278-288. <https://doi.org/10.1016/j.biombioe.2017.11.015>
- 497 Cengiz MF, M Catal, F Erler & AK Bilgin (2014) Rapid and sensitive determination of the prochloraz residues  
498 in the cultivated mushroom, *Agaricus bisporus* (Lange) Imbach. *ANAL METHODS-UK* 6:1970-1976.  
499 <https://doi.org/10.1039/c3ay42293c>
- 500 Chen YR (1981) Impeller Power Consumption in Mixing Livestock Manure Slurries. *Transactions of the ASAE*  
501 *American Society of Agricultural Engineers* 24:0187-0192.
- 502 Dapelo D, F Alberini & J Bridgeman (2015) Euler-Lagrange CFD modelling of unconfined gas mixing in  
503 anaerobic digestion. *WATER RES* 85:497-511. <https://doi.org/10.1016/j.watres.2015.08.042>
- 504 Ding J, X Wang, X Zhou, N Ren & W Guo (2010) CFD optimization of continuous stirred-tank (CSTR) reactor  
505 for biohydrogen production. *BIORESOURCE TECHNOL* 101:7005-7013.  
506 <https://doi.org/10.1016/j.biortech.2010.03.146>
- 507 Esen M & T Yuksel (2013) Experimental evaluation of using various renewable energy sources for heating a  
508 greenhouse. *ENERG BUILDINGS* 65:340-351. <https://doi.org/10.1016/j.enbuild.2013.06.018>
- 509 Fleming B & J Graham (2002) Novel simulation of anaerobic digestion using computational fluid dynamics  
510 Book Novel simulation of anaerobic digestion using computational fluid dynamics.
- 511 Gronowska M, S Joshi & HL MacLean (2009) A REVIEW OF US AND CANADIAN BIOMASS SUPPLY  
512 STUDIES. *BIORESOURCES* 4:341-369.
- 513 Hassan M, C Zhao & W Ding (2020) Enhanced methane generation and biodegradation efficiencies of goose  
514 manure by thermal-sonication pretreatment and organic loading management in CSTR. *ENERGY* 198.  
515 <https://doi.org/10.1016/j.energy.2020.117370>
- 516 Hooshyar N, J Ommen, PJ Hamersma, S Sundaresan & RF Mudde (2013) Dynamics of Single Rising Bubbles  
517 in Neutrally Buoyant Liquid-Solid Suspensions. *PHYS REV LETT* 110:244501-244501.
- 518 Kumarappan S, S Joshi & HL MacLean (2009) BIOMASS SUPPLY FOR BIOFUEL PRODUCTION:  
519 ESTIMATES FOR THE UNITED STATES AND CANADA. *BIORESOURCES* 4:1070-1087.
- 520 Leow CW, CP Bong, LS Chua, II Muhamad, CT Lee, C Li & JJ Klemes (2020) Feasibility Study of Composting  
521 and Anaerobic Digestion Plant at Community Scale in Malaysia. *WASTE BIOMASS VALORI* 11:5165-5173.  
522 <https://doi.org/10.1007/s12649-019-00894-5>
- 523 Luan D, Q Chen & S Zhou (2014) Numerical Simulation and Analysis of Power Consumption and Metzner-Otto  
524 Constant for Impeller of 6PBT. *CHINESE JOURNAL OF MECHANICAL ENGINEERING* 27:635-640.  
525 <https://doi.org/10.3901/CJME.2014.03.635>
- 526 Luo T, Y Long, J Li, X Meng, Z Mei, E Long & B Dai (2015) Performance of a Novel Downward Plug-Flow  
527 Anaerobic Digester for Methane Production from Chopped Straw. *BIORESOURCES* 10:943-955.
- 528 Marti-Herrero J, R Alvarez, MR Rojas, L Aliaga, R Cespedes & J Carbonell (2014) Improvement through low  
529 cost biofilm carrier in anaerobic tubular digestion in cold climate regions. *BIORESOURCE TECHNOL* 167:87-  
530 93. <https://doi.org/10.1016/j.biortech.2014.05.115>

531 Mendoza AM, TM Nez, VM Ana & L Amparo (2011) Modeling flow inside an anaerobic digester by CFD  
532 techniques. *International Journal of Energy & Environment* 2.

533 Moghtaderi B, C Sheng & TF Wall (2006) AN OVERVIEW OF THE AUSTRALIAN BIOMASS  
534 RESOURCES AND UTILIZATION TECHNOLOGIES. *BIORESOURCES* 1:93-115.

535 Moretto G, F Ardolino, A Piasentin, L Girotto & F Cecchi (2020) Integrated anaerobic codigestion system for  
536 the organic fraction of municipal solid waste and sewage sludge treatment: an Italian case study. *J CHEM*  
537 *TECHNOL BIOT* 95:418-426. <https://doi.org/10.1002/jctb.5993>

538 Munoz R, C Soto, C Zuniga & S Revah (2018) A systematic comparison of two empirical gas-liquid mass  
539 transfer determination methodologies to characterize methane biodegradation in stirred tank bioreactors. *J*  
540 *ENVIRON MANAGE* 217:247-252. <https://doi.org/10.1016/j.jenvman.2018.03.097>

541 Paul EL, VA Atiemo-Obeng & SM Kresta (2004) *Handbook of industrial mixing :science and practice*. Hoboken,  
542 N.J. Wiley-Interscience:1377.

543 Villamil JA, AF Mohedano, J San Martin, JJ Rodriguez & MA de la Rubia (2020) Anaerobic co-digestion of the  
544 process water from waste activated sludge hydrothermally treated with primary sewage sludge. A new approach  
545 for sewage sludge management. *RENEW ENERG* 146:435-443. <https://doi.org/10.1016/j.renene.2019.06.138>

546 Wu B (2010) CFD simulation of gas and non-Newtonian fluid two-phase flow in anaerobic digesters. *WATER*  
547 *RES* 44:3861-3874. <https://doi.org/10.1016/j.watres.2010.04.043>

548 Wu B (2011) CFD investigation of turbulence models for mechanical agitation of non-Newtonian fluids in  
549 anaerobic digesters. *WATER RES* 45:2082-2094. <https://doi.org/10.1016/j.watres.2010.12.020>

550 Wu B (2011) CFD investigation of turbulence models for mechanical agitation of non-Newtonian fluids in  
551 anaerobic digesters. *WATER RES* 45:2082-2094. <https://doi.org/10.1016/j.watres.2010.12.020>

552 Wu B (2013) Advances in the use of CFD to characterize, design and optimize bioenergy systems. *COMPUT*  
553 *ELECTRON AGR* 93:195-208. <https://doi.org/10.1016/j.compag.2012.05.008>

554 Yang Y, J Xia, J Li, J Chu, L Li, Y Wang, Y Zhuang & S Zhang (2012) A novel impeller configuration to  
555 improve fungal physiology performance and energy conservation for cephalosporin C production. *J*  
556 *BIOTECHNOL* 161:250-256. <https://doi.org/10.1016/j.jbiotec.2012.07.007>

557 Zou X, J Xia, J Chu, Y Zhuang & S Zhang (2012) Real-time fluid dynamics investigation and physiological  
558 response for erythromycin fermentation scale-up from 50 L to 132 m<sup>3</sup> fermenter. *BIOPROC BIOSYST ENG*  
559 35:789-800. <https://doi.org/10.1007/s00449-011-0659-z>

560